Nanoscale

Scheme 1. Scheme of frogspawn-inspired hierarchical porous $NaTi_2(PO_4)_3$-C array. Both SEM images are the arrays with different magnifications.

high-efficiency oxygen permeability and ensure the well-balanced breath of each spawn in the array. Therefore, two important advantages of the frogspawn array, *i.e.* the porous morphology with large surface area and the unique functionality of high-efficient mass exchange, offer great inspiration for us to design electrode materials for high-power applications.

Following this viewpoint, for the first time, we report the design of a new frogspawn-like architecture for $NaTi_2(PO_4)_3$ via a facile impregnation process. The strategy can also be applied to other materials such as polyanions, oxides, fluorides, et al. as well. The carbon-based framework ensures fast electron transport, and 3D hierarchical porous array enables easy electrolyte penetration and fast ion transport. Moreover, the basic "core-shell" structure offsets the insufficient volumetric energy density, which is the fatal defect in porous architecture. As applied in aqueous sodium ion battery, the frogspawn-inspired anode exhibits superior high rate capacity and excellent cycling stability. Moreover, the $NaTi_2(PO_4)_3/Na_{0.44}MnO_2$ full cell displays ultralong cycling property and favorable high rate capability, demonstrating the superiority of the frogspawn-inspired structure.

2 Experimental

2.1 Synthesis

Preparation of hollow carbon sphere. 2 mL ammonia aqueous solution (25 wt.%), 30 mL ethanol and 20 mL DI water were mixed well to form a mixed solution. Then 2.5 mL tetraethylorthosilicate (TEOS) and 10 mL ethanol were added to above solution under magnetic stirring, followed by addition of 0.3 g resorcinol and 0.45 g formaldehyde solution. The mixture was strongly stirred for one day at ambient temperature. Then it was sealed in an autoclave and heated at 100 °C for 24 hours. The obtained gel was washed and dried in a vacuum oven at 80 °C overnight and heated at 900 °C for 2 hours in Ar atmosphere. Finally, the carbon sphere was etched by HF solution (10 wt.%) for one day and washed by DI water until pH value of filtrate reaches 7.

Preparation of $NaTi_2(PO_4)_3$ precursor. Stoichiometric amount of tetrabutyl titanate was dissolved into hydrogen peroxide (30 wt%) solution under vigorously stirring. Then ammonia solution (25 wt.%) was added into above solution, followed by citric acid and the mixture of sodium bicarbonate and ammonium dihydrogen phosphate. Subsequently, glycol was added to the mixture and kept stirring at 80 °C for 40 hours. The obtained transport concentrated solution was used as precursor solution.

Construction of frogspawn-inspired $NaTi_2(PO_4)_3$-carbon array and reference samples. The preform impregnation process was carried out in a lab-assembled system (Figure S1). Firstly, desirable amount of hollow carbon sphere was placed in the sealed glass vessel. Then the $NaTi_2(PO_4)_3$ precursor solution was slowly added to the hollow carbon sphere with vacuum in between to ensure the effective impregnation. The whole impregnation system was kept at 80 °C to enable slowly drying of the mixture. After impregnation process, the intermediate product was annealed at 700 °C for 8 hours at a heating rate of 2 °C·min^{-1} in Ar atmosphere. For comparison, two reference samples were prepared. Firstly, the $NaTi_2(PO_4)_3$ precursor solution was directly dried at 80 °C overnight to produce the dry gel. Then it was sintered at 800 °C for 10 hours in air to obtain the carbon-free reference sample (CF-R). Then the CF-R sample was mixed with desirable amount of sucrose and sintered at 800 °C for 2 hours in Ar atmosphere to obtain carbon-coated reference sample (CC-R).

2.2 Characterization

Powder X-ray diffraction (XRD, Bruker D8/Germany) using Cu Kα radiation was employed to identify the crystalline phase of the material. The experiment was performed by using step mode with a fixed time of 3 s and a step size of 0.02o. The XRD pattern was refined by using the Rietveld method. The morphology was observed with a scanning electron microscope (SEM, HITACHIS-4700) and a transmission electron microscope (TEM, JEOS-2010 PHILIPS). Nitrogen adsorption-desorption isotherms were measured using a Micro- meritics ASAP 2010 sorptometer and specific surface and pore size distribution were calculated correspondingly. Carbon contents of the samples were determined by an element analyzer (EA, Elementar Vario EL).

2.3 Electrochemical measurements

Each composite electrode was made from a mixture of the active material, carbon black and polytetrafluoroethylene (PTFE) in a weight ratio of 80:10:10. The mixture was pressed into nickel foam and then dried at 80 °C for 12 hours in air. The effective area of each electrode is 1 cm^2. The de/intercalation mechanism of sodium ion was evaluated in 1M Na_2SO_4 electrolyte with Ag/AgCl as reference. The aqueous rechargeable sodium battery was assembled using $Na_{0.44}MnO_2$ as cathode and $NaTi_2(PO_4)_3$ composite as anode. The loading of the active materials of the cathode are *ca.* 4~6 mg·cm^{-2}, and that of the anode are *ca.* 2~3 mg·cm^{-2}. The Ag/AgCl electrode was employed as a reference electrode to monitor the potential of each electrode upon galvanostatic cycling of the full cell. Cyclic voltammetry (CV) and electrochemical impedance spectroscopy (EIS) were measured a Zivelab electrochemical workstation. Galvanostatic
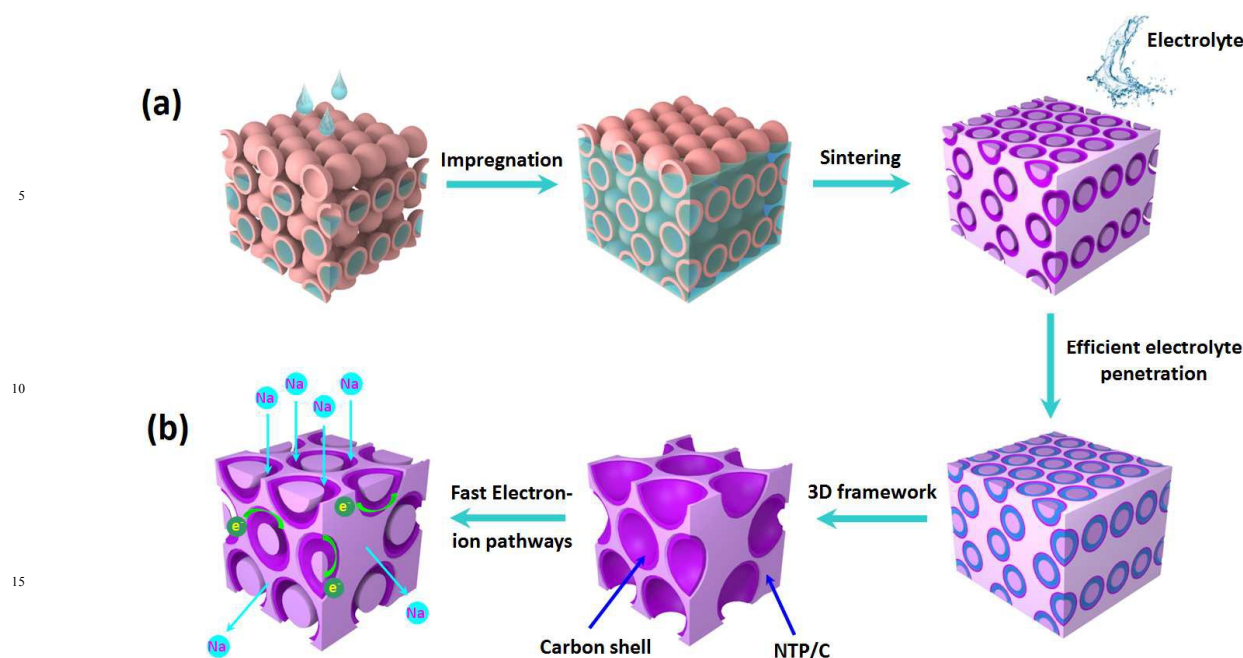
Figure 1 (a) Schematic fabrication process for the frogspawn-inspired $NaTi_2(PO_4)_3$-C array, which involves the preform impregnation and sintering steps. (b) Schematic illustration of the structure for the frogspawn-inspired array. The partially enlarged image emphasizes the surface carbon shell and the $NaTi_2(PO_4)_3$/C skeleton of the 3D hollow framework. The high efficient electrolyte penetration and electron/ion transport pathways are illustrated.

tests were conducted on a LAND battery testing system (Wuhan, China).

3   Results and Discussion

The main process to prepare the frogspawn-inspired $NaTi_2(PO_4)_3$-C array is based on a preform impregnation process as illustrated in Figure 1(a). Firstly, a concentrated solution of $NaTi_2(PO_4)_3$ precursor is vacuum infiltrated into the highly porous hollow carbon sphere. The carefully controlled synthetic conditions, including slowly syringe speed, strong vacuum and simultaneous drying ensures the sufficient impregnation of solution into the voids of hollow carbon sphere. After the all the voids are filled, the precursor solution comes to the gaps between the carbon spheres subsequently. Then, in the following sintering process, the precursor decomposes to $NaTi_2(PO_4)_3$/C accompanying release of sub-produced gases. The wall of hollow carbon spheres were connected by internal $NaTi_2(PO_4)_3$ skeleton and construct the framework of the 3D array. Meanwhile, the cores of hollow carbon spheres contract and exuviate from the carbon shells, forming the core $NaTi_2(PO_4)_3$ nanospheres.

Both the "shell-core" basic unit and the 3D porous framework construct $NaTi_2(PO_4)_3$-C arrays. As illustrated in Figure 1b, they are similar to frogspawns on both morphology and functionality. The first is their similar morphology. The frogspawns are composed of "core-shell" basic units and the architecture of $NaTi_2(PO_4)_3$ nanosphere filled in the hollow array is similar to the spawn core inside the jelly shell. Furthermore, they have similar functionality. The most important character of frogspawn inspired us is its facile oxygen impregnation.

Similarly, the produced array has hierarchical pores and interconnective channels, which enables easy electrolyte penetration and promotes fast ion transport. At the same time, the carbon shells build continuous pathways for fast electron transport. Both facile electron/ion transport pathways ensure superior sodium intercalation for the composite. Moreover, similar to the good toughness of frogspawn in nature, the favorable durability ensures superior stability of $NaTi_2(PO_4)_3$-C array during cycling.

The morphology and microstructure of the prepared frog spawn-inspired $NaTi_2(PO_4)_3$-C array are investigated by SEM and TEM observations. As displayed in Figure 2a, the material exhibits three-dimensional porous architecture in large microsize-scale. The low-magnification SEM observation (Figure 2b) evidences the existence of uniform shell-core units inside the array. The enlarged SEM and TEM images (Figure 2c,d) demonstrate the pores in the size of ca. 200 nm uniformly distribute inside the array. The nanospheres in the range of 100~150 nm are embedded in the hollow pores, which constructs the "core-shell" units and results in the frogspawn-type structure. Furthermore, the element mapping images (Figure 2e) evidence the uniform distribution of Na, Ti and P in the $NaTi_2(PO_4)_3$ array.

More detailed structure of the "core-shell" unit is further indentified by HRTEM images (Figure 2f and g). The "core" nanosphere has distinct fringe of $NaTi_2(PO_4)_3$, which clearly confirms its single crystal nature. The "shell" of the unit is composed of the bulk skeleton and the surface layer, as illustrated in Figure 2h. The well-resolved lattice fringe with an interplanar distance of 0.61 nm corresponds to the (012) lattice planes of the
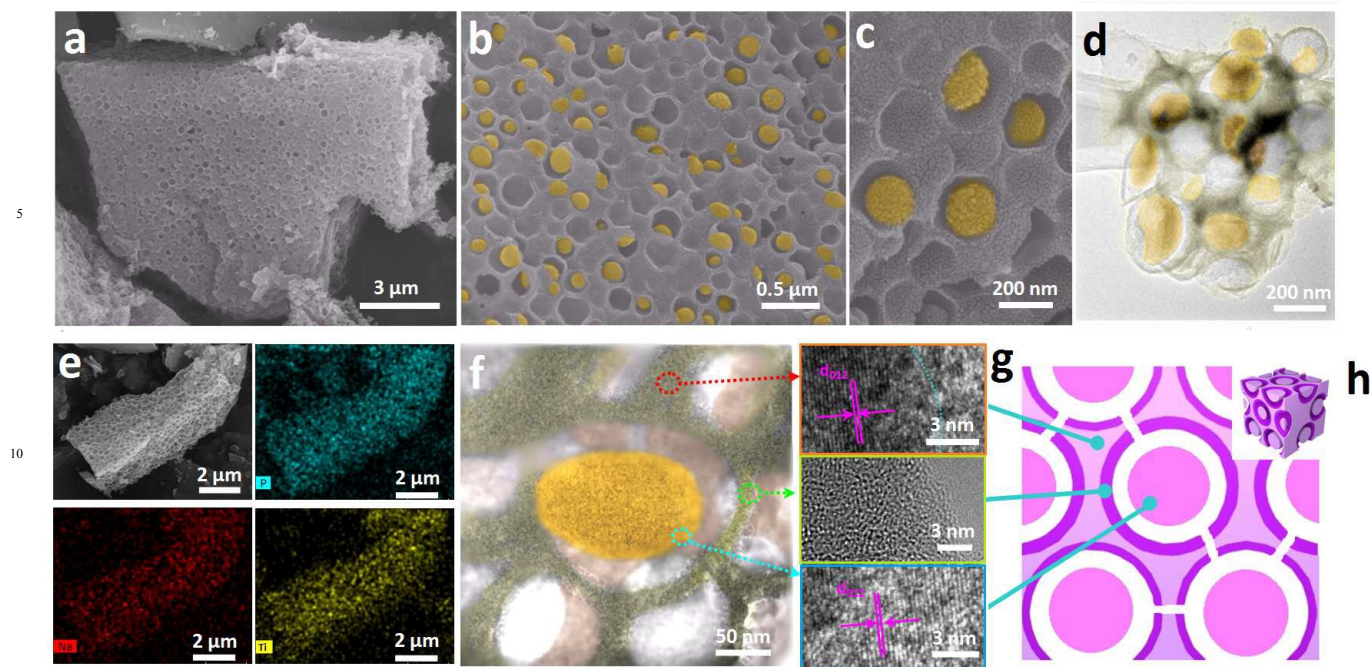
Figure 2 (a) Morphologies of the frogspawn-inspired NaTi$_2$(PO$_4$)$_3$-C array: (a) SEM image of the 3D hierarchical porous array, enlarged SEM (b, c) and TEM (d) images of the shell-core structure inside the array, (e) elements (Na, Ti, P) mapping of the prepared composite, (f) TEM of one basic unit and the HRTEM images corresponding to the bulk and surface of the shell, and the core nanosphere is emphasized in g. The schematic images of a basic "shell-core" unit and the whole 3D array is illustrated in h.

NaTi$_2$(PO$_4$)$_3$, which confirms the single crystal nature of the skeleton. The surface layer arising from the hollow carbon sphere is amorphous, which has the thickness of 10 nm. It builds 3D conductive layer for the framework and provides fast electron transport pathways for the composite. Moreover, the voids in the carbon shell arising from the crack of carbon sphere provides interconnection between the pores of the array, which facilitate high-efficient electrolyte percolation in the whole array. Therefore, all of the advantages of the NaTi$_2$(PO$_4$)$_3$-C array, including the "shell-core" structure, high-conductive framework and the interconnective voids facilitate fast electron/ion transport, which is similar to the facile oxygen impregnation capability of frogspawn.

The porous structure of the prepared NaTi$_2$(PO$_4$)$_3$-C array is further characterized by nitrogen sorption isotherms. As displayed in Figure 3a, the significant hysteresis loop confirms the high porous structure of the array, which possesses a high specific surface area of 94.2 m^2 g^{-1} and a large pore volume of 0.43 cm^3 g^{-1}. Figure 3b displays the pore size distribution of the composite. Obvious bimodal porosity is observed, *i.e.* ~2.8 nm mesopores (2~50 nm) arising from the pores in the carbon shell and ~70 nm macropores (>50 nm) associated with the voids in the framework of the array. The results confirm the hierarchical porous structure of prepared composite, which are coincided with above SEM and TEM observation results.

The durability of the frogspawn-inspired array is investigated by characterizing the carbon matrix of the NaTi$_2$(PO$_4$)$_3$-C array. The pure carbon matrix is obtained by treating the prepared array with HF etching in intermittent ultrasonic treatment. The EDX results confirm that all of the NaTi$_2$(PO$_4$)$_3$ has been removed and only carbon element remains (Figure s2). A continuous and porous carbon matrix is observed in the SEM observation (Figure 4a), and TEM image (Figure 4b) evidences the existence of interconnected residual carbon between the hollow carbon spheres. The good durability of carbon matrix is evidenced by
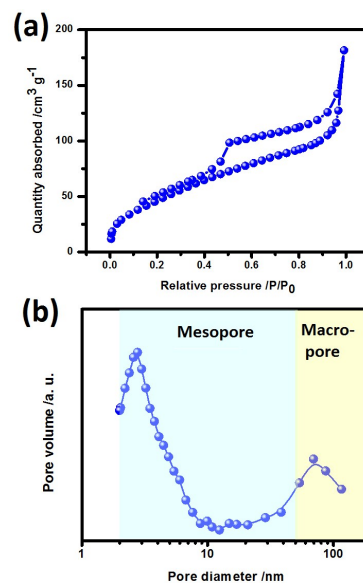
Figure 3 (a) N$_2$ sorption isotherms and (b) pore size distribution of the frogspawn-inspired NaTi$_2$(PO$_4$)$_3$-C array.
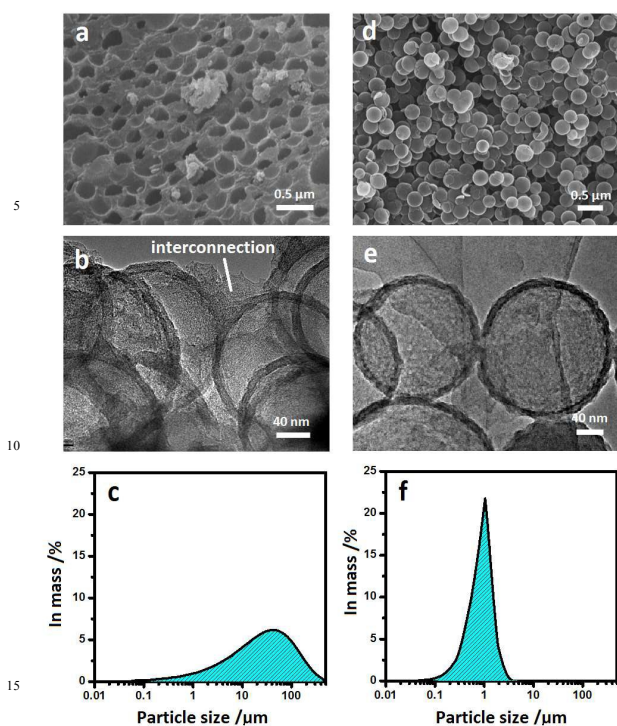
Figure 4 Morphologies (a, b, d, e) and particle size distributions (c, f) of the pure carbon matrix in the frogspawn-inspired array (a, b, c) and the pristine hollow carbon sphere (d, e, f).

particle size distribution analysis. After high-power ultrasonication, the carbon matrix still maintains the large aggregated state in larger particle size (Figure 4c). On the contrary, the pristine hollow carbon sphere (Figure 4d,e), which has slight agglomeration, can be easily broken into individual one by ultrasonication and only smaller particle size is observed (Figure 4f). Therefore, the good durability of the hierarchical porous array ensures its excellent stability during cycling, which is similar to the superior toughness of frogspawn in nature.

The crystal structure of the $NaTi_2(PO_4)_3$-C array is identified by X-ray diffraction (XRD). All of the diffraction peaks can be readily indexed to the NASICON structure in the $R\bar{3}c$ space group, which suggests the high purity of prepared material. Rietveld refinement is carried out to more precisely estimate the $NaTi_2(PO_4)_3$ phase (Figure 5). All of the obtained lattice parameters and atomic parameters are listed in Table s1, which are coincided with previous reported values.[14-17] As illustrated in Figure 5b, the basic unit of $[Ti_2(PO_4)_3]$ framework is constructed by two TiO_6 octahedra and three PO_4 tetrahedra via corner sharing and sodium ions fully occupy the interstitial sites. The 3D framework of $NaTi_2(PO_4)_3$ crystal not only provides the large interstitial spaces for sodium accommodation, but also offers open channels for ion transport. Therefore, $NaTi_2(PO_4)_3$ is a good candidate in sodium hosts.

The sodium intercalation chemistry of the frogspawn-inspired array is investigated. For comparison, two reference samples, *i.e.* the carbon-free sample (CF-R) and simple carbon coated sample
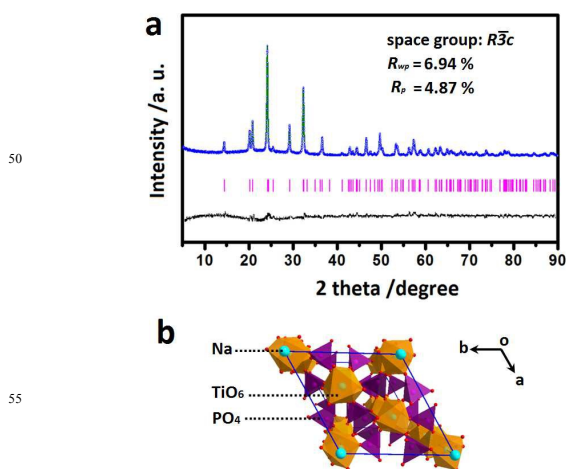
Figure 5 (a) XRD pattern of the $NaTi_2(PO_4)_3$-C array. (b) Schematic illustration of the crystal structure of $NaTi_2(PO_4)_3$.

(CC-R) were also employed. Their physical characteristics are summarized in Table S2. XRD patterns (Figure s3) demonstrate the single phase structure of both references samples. The low surface areas of reference samples are associated with their large solid aggregated particles (Figure s4).

Firstly, CV measurements are carried out on all of the samples. One pair of redox peaks is observed for all samples, corresponding to the sodium insertion/extraction reaction in the $NaTi_2(PO_4)_3$ crystal. The frogspawn-inspired array exhibits stronger redox peaks and smaller peak potential differences than the reference samples, indicating its better redox reversibility and superior sodium intercalation kinetics (Figure 6a).[25-27]

A more detailed investigation is carried out by Electrochemical Impedance Spectroscopy (EIS). Figure 6b and c illustrates the Nyquist plots of frogspawn-inspired array recorded at different potentials from -0.5~-1.0 V (vs. Ag/AgCl). The spectra consist of the arc in the high frequency and the inclined line in low frequency. The high frequency part is attributed to the charge (electron) injection across the interface of the electrode material. And the low frequency part corresponds to the solid-state diffusion of sodium ion.[28,29] The charge transfer resistance (R_{ct}) can be obtained based on the high frequency part. As displayed in Figure 6d, the R_{ct} values change as the electrode potential decreases. Thus the whole range of R_{ct} values can be divided into two regions, *i.e.* initially almost constant at high potential (region I), and then turn to increase with decreasing the electrode potential (region II). In the first region, the initially constant and low charge transfer resistance is associated with the fast react rate of surface defects present in the array.[30,31] In the second region, after the consumption of surface defects, the reaction propagates deeper into the bulk of the material, which leads to a lower rate and a higher R_{ct} value. Compared with the reference samples, the frogspawn-inspired array exhibits longer range with lower R_{ct} values in region I, suggesting its faster rate of surface reaction. Moreover, the frogspawn-inspired array
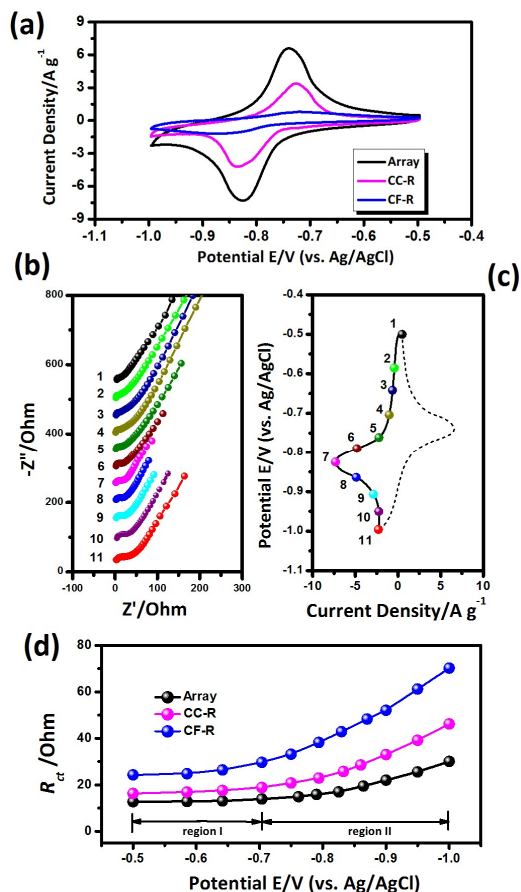
Figure 6 (a) CV curves of the frogspawn-inspired array, carbon coated (CC-R) and carbon free (CF-R) reference samples at the scan rate of 2 mV s^{-1}. (b) Nyquist plots of the frogspawn-inspired array at different potentials displayed in c. (d) the calculated R_{ct} values of all the samples. Two different regions of R_{ct} values for the frogspawn-inspired array are illustrated in d.

displays the slowest increasing rate of R_{ct} value among the samples in region II, certifying its faster rates of bulk reaction. The results demonstrate the superior electrochemical kinetics of frogspawn-inspired array. It can be attributed to its hierarchical porous structure and 3D conductive framework, which facilitate the fast charge (electron) transfer reaction and result in the lower R_{ct} values.

Motivated by the improved electrochemical kinetics, the rate capability and cycling stability of the frogspawn-inspired array are investigated. A series of current densities, from 0.5 C to 90 C, are employed to evaluate the rate capability. As displayed in Figure 7a, the frogspawn-inspired array exhibits obvious higher capacity than reference samples at all current densities. As the current density increases, the difference between the array and references become more significant (Figure 7b). Moreover, the frogspawn-inspired array also exhibits better cycling properties than the reference samples, indicating the improved stability of the unique architecture during cycling.

In order to further investigate the cycling performance of the frogspawn-inspired array, the low- (1 C) and high-rate (20 C) long-term cycling measurements are carried out. As displayed in Figure 7c and d, low coulombic efficiencies are observed at both rates during initial a few cycles. It is associated with the hydrogen evolution at low voltage and similar phenomenon has also been detected in previous reports.[15,32-35] At both rates, the coulombic efficiencies increase and the capacities decrease as increasing cycle number. At the end of cycling, the frogspawn-inspired array retains 89% (at 20 C, 2000 cycles) and 88% (at 1 C, 400 cycles) of its initial capacity with nearly 100% coulombic efficiency.

To clarify the superiority of the frogspawn-inspired array, its electrochemical performance is compared with previously reported results. As compared in Table S3, both the high rate capability and the cycling property of the frogspawn-inspired
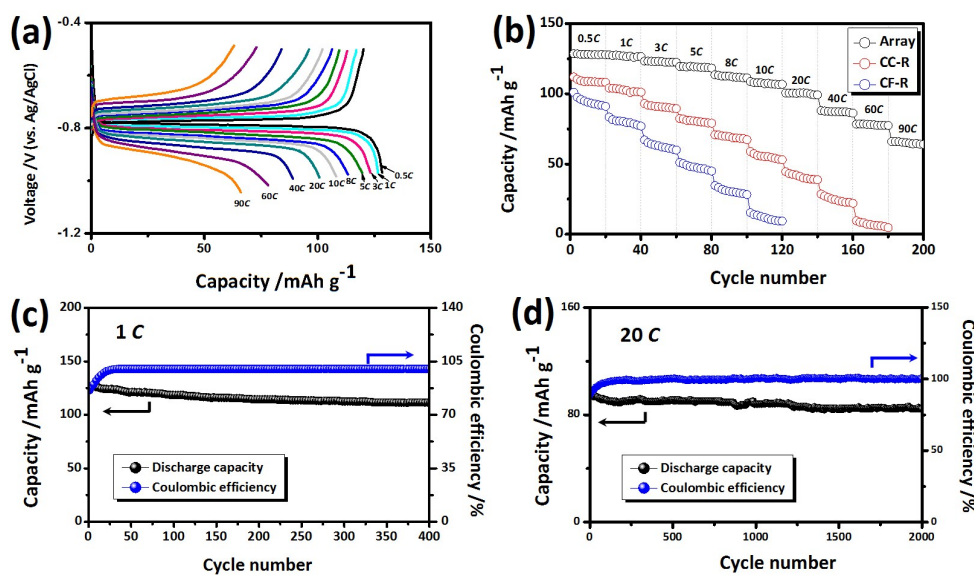
Figure 7 (a) Charge/discharge curves of the frogspawn-inspired NaTi$_2$(PO$_4$)$_3$ array at different rates. (b) Comparison of the rate capability of the frogspawn-inspired array and the references samples at the rate from 0.5 to 90 C. Long-term cycling performance of the frogspawn-inspired array at 1C for four hundreds cycles (c) and at 20 C for two thousand cycles (d).
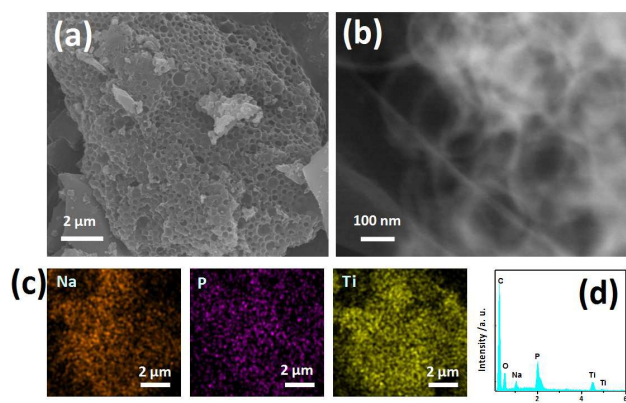
Figure 8 Morphology of the frogspawn-inspired $NaTi_2(PO_4)_3$ array after cycles: (a) SEM and (b) bright-field TEM images, (c) Na, P, Ti element mapping, and (d) EDS analysis results.

array are superior to the previous reported results.[15,32-35] The improvements are associated with its rigid and stable framework, which facilitates long-term cycling and enables fast electron/ion transport.

The morphology of the frogspawn-inspired array after cycling is investigated by SEM and bright-field TEM observations. As displayed in Figure 8a and b, the sample maintains its architecture after cycling. Its three-dimensional framework and hierarchical porous architecture still exist, which demonstrates its good structural stability. Moreover, the EDS results (Figure 8c and d) suggest the homogenous distribution of the Ti, P and Na elements with desirable atomic ratio (Na: Ti: P=1: 2: 3). Therefore, all of the advantages of the frogspawn-

inspired array, including the high stable framework, hierarchical porous structure and fast electron/ion transport capability, result in its superior electrochemical performance.

Inspired by the superior properties of frogspawn-inspired structure, a full aqueous sodium battery is assembled based on the anode of prepared $NaTi_2(PO_4)_3$ array, the cathode of $Na_{0.44}MnO_2$, and the electrolyte of Na_2SO_4. The weight ratio of the anode and cathode active material is *ca.* 1: 2.5~2.7. The capacity of the full cell is calculated based on the total mass of both cathode and anode active material. In order to investigate the potentials of both electrodes, a reference electrode of Ag/AgCl is employed. The typical charge/discharge curves of individual electrodes and full cell at 0.5 *C* are displayed in Figure 9a and b. The flat plateaus of $NaTi_2(PO_4)_3$ anode are associated with the redox reaction of Ti^{3+}/Ti^{4+}, and the three plateaus of $Na_{0.44}MnO_2$ are associated with its phase transitions during sodium intercalation.[36] The discharge curves of the full cell at different rates are displayed in Figure 9c. As the current density increases, the capacity decreases correspondingly. Even at high current density of 60 *C*, the cell still delivers 67% of the capacity of 3 *C*, demonstrating its good high rate capability. Moreover, the long-term cycling performance of the full cell at both low (1 *C*) and high rates (10 and 60 *C*) are investigated. As displayed in Figure 9d and e, it is capable of long term cycling at both rates, which retains 70% of the capacity after 1000 cycles at alternate 10 C and 60 C and retains 84% of the capacity after 500 cycles at 1 *C* with nearly 100% coulombic efficiency. The results demonstrate the ultrafast charge/discharge capability and ultralong cycling stability of present cell, which is superior in the state-of-art aqueous sodium ion batteries. Therefore, the results demonstrate that the frogspawn-inspired architecture is a new strategy to
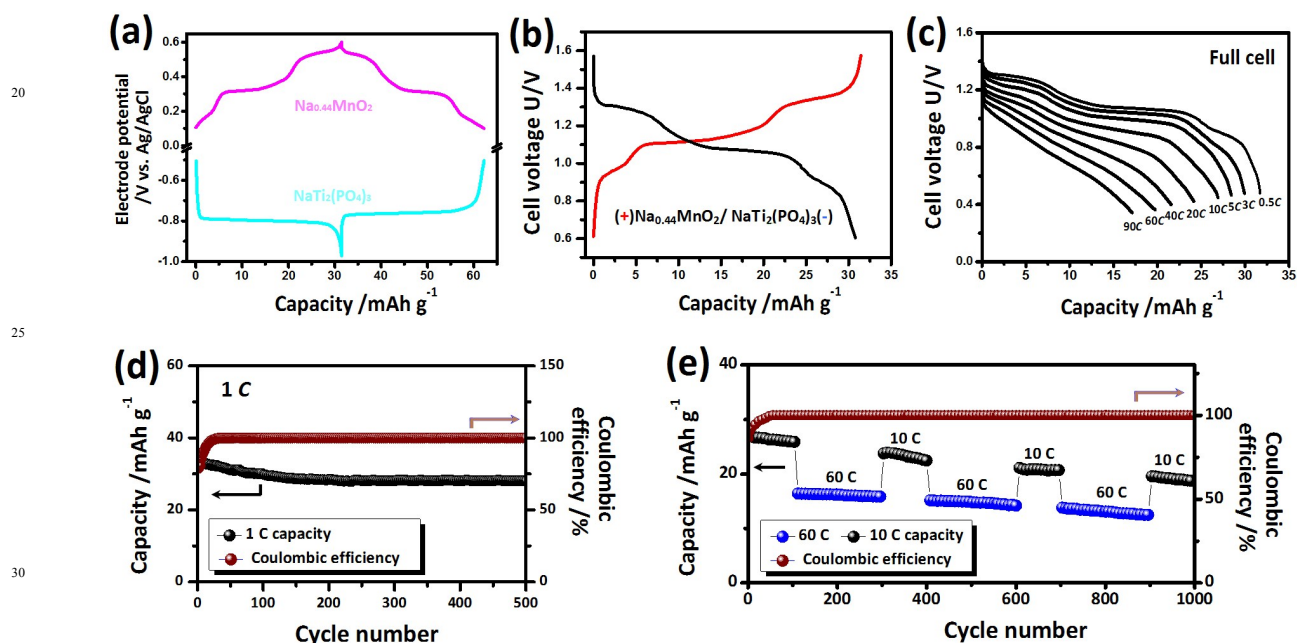
Figure 9 Charge/discharge curves of (a) individual $Na_{0.44}MnO_2$ cathode, frogspawn-inspired $NaTi_2(PO_4)_3$ anode and (b) the full cell at 0.5 C. (c) Rate capability of the cell at different current densities. Long-term cycling performance of the cell at 1 C for five hundreds cycles (d) and at alternate 10 and 60 C for one thousand cycles (e). The capacity of the full cell is calculated based on the total mass of both anode and cathode active material.

fabricate high-performance electrode materials in high-power applications.

4 Conclusions

In summary, we have demonstrated the successful design and fabrication of a new architecture, named "frogspawn-inspired hierarchical porous array", which has a wide range of applications in energy storage devices. Based on the "shell-core" units, the hierarchical porous array can be easily prepared by a preform impregnation strategy. The network of the array is formed by the hollow carbon shell, which is connected by the electrochemical active skeleton. The core nanospheres are residual in voids of hollow array, constructing the frogspawn-type architecture. The unique structure enables high-efficient electron/ion transport and excellent durability, which makes it suitable for high power applications. As a case study, the frogspawn-inspired $NaTi_2(PO_4)_3$-C array is prepared. It exhibits superior high rate capacity and excellent cycling stability when applied as anode in ARSB. Moreover, the $Na_{0.44}MnO_2$/ $NaTi_2(PO_4)_3$ array full cell is capable of high-rate long-term cycling, which is among the best of state-of-art aqueous sodium ion systems. Therefore, the frogspawn-inspired structure and impregnation fabrication strategy provide a new idea for tailored design of electrodes in high-power applications.

Acknowledgement

Notes and references

aKey Laboratory for Photonic and Electronic Bandgap Materials, Ministry of Education; College of Chemistry and Chemical Engineering, Harbin Normal University, Harbin, 150025, Heilongjiang, China; E-Mail: chaodenghsd@sina.com
bKey Laboratory of Superlight Material and Surface Technology, Ministry of Education, College of Material Science and Chemical Engineering, Harbin Engineering University, Harbin 150001, Heilongjiang, China; E-Mail: senzhang@hrbeu.edu.cn

†Electronic Supplementary Information (ESI) available: Lab-assembled preform impregnation system; EDX spectroscopy of the residual carbon matrix after HF treatment; Atomic parameters and lattice parameters of the prepared array; crystal structural, morphological and physical characteristics of the reference samples, comparison of the electrochemical performance between the frogspawn-inspired array and the previous reported results. See DOI: 10.1039/b000000x/

1   J. M. Tarascon, M. Armand, *Nature* **2001**, *4*, 359-367.

2   C. Deng, S. Zhang, *ACS Appl. Mater. Interfaces* **2014**, *6*, 9111-9117.

3   N. Yabuuchi, K. Kubota, M. Dahbi, S. Komaba, *Chem. Rev.* **2014**, *114*, 11636-11682.

4   S. Zhang, C. Deng, Y. Meng, *J. Mater. Chem. A* **2014**, *2*, 20538-20544.

5   H. Kim, J. Hong, K. Park, H. Kim, S. Kim, K. Kang, *Chem. Rev.* **2014**, *114*, 11788-11827.

6   M. Pasta, C. D. Wessells, R. A. Huggins, Y. Cui, *Nat. Commun.* **2012**, *3*, 1149-1153.

7   U. Kohler, C. Antonius, P. Bauerlein, *J. Power Sources* **2004**, *127*, 45-52.

8   W. Li, J. R. Dahn, D. S. Wainwright, *Science* **1994**, *264*, 1115-1118.

9   C. Deng, S. Zhang, Y. X. Wu, *Nanoscale* **2015**, *7*, 487-491.

10   C. Deng, S. Zhang, Z. Dong, Y. Shang, *Nano Energy* **2014**, *4*, 49-55.

11   S. Li, Y. F. Dong, L. Xu, X. Xu, L. He, L. Q. Mai, *Adv. Mater.* **2014**, *26*, 3545-3553.

12   X. Wu, M. Sun, Y. Shen, J. Qian, Y. Cao, X. Ai, H. Yang, *ChemSusChem* **2014**, *7*, 407-411.

13   X. Y. Wu, Y. L. Cao, X. P. Ai, J. F. Qian, H. X. Yang, *Electrochem. Commun.* **2013**, *31*, 145-148.

14   Z. G. Hou, X. N. Li, J. W. Liang, Y. C. Zhu, Y. T. Qian, *J. Mater. Chem. A,* **2015**, *3*, 1400-1404.

15   W. Wu, A. Mohamed, J. F. Whitacre, *J. Electrochem. Soc.* **2013**, *160*, A497-A504.

16   C. Wu, P. Kopold, Y. Ding, P. Aken, J. Maier, Y. Yu, *ACS Nano* **2015**, *6*, 6610-6618.

17   B. D. Zhao, Q. Y. Wang, S. Zhang, C. Deng, *J. Materials Chemistry A* **2015**, *3*, 12089-12096.

18   Z. Li, D. Young, K. Xiang, W. C. Caeter, Y. M. Chiang, *Adv. Energy Mater.* **2013**, *3*, 290-294.

19   Z. Wang, F. Jiang, Y. Zhang, Y. You, Z. Wang, Z. Guan, *ACS nano* **2015**, *9*, 271-278.

20   A. J. Svagan, D. Busko, Y. Aviasevich, G. Glasser, S. Baluschev, K. Landfester, *ACS nano* **2014**, *8*, 8198-8207.

21   S. Wang, S. Chen, Q. Wei, X. Zhang, S. Wong, S. Sun, X. Li, *Chem. Mater.* **2015**, *27*, 336-342.

22   D. B. Xiong, M. Cao, Q. Guo, Z. Tan, G. Fan, Z. Li, D. Zhang, *ACS Nano* **2015**, *9*, 6934-6943.

23   D. Y. Chung, K. J. Lee, S. H. Yu, M. Kim, S. Y. Lee, O. H. Kim, H. J. Park, Y. E. Sung, *Adv. Energy Mater.* **2015**, *5*, 1401309-1401317.

24   Q. Yang, S. Zhu, W. Peng, C. Yin, W. Wang, J. Gu, W. Zhang, J. Ma, T. Deng, C. Feng, D. Zhang, *ACS Nano* **2013**, *7*, 4911-4918.

25   L. Tan, S. Zhang, C. Deng, *J. Power Sources* **2015**, *275*, 6-13.

26   S. Zhang, C. Deng, H. Gao, F. L. Meng, M. Zhang, *Electrochim. Acta* **2013**, *107*, 406-412.

27   S. Y. Yang, S. Zhang, B. L. Fu, Q. Wu, F. L. Liu, C. Deng, *J Solid State Electrochem.* **2011**, *15*, 2633-2638.

28   A. J. Bard, L. R. Faulkner, Electrochemical methods, 2nd ed., Wiley. New York, 2001.

29   Q. Y. Wang, B. D. Zhao, S. Zhang, X. H. Gao, C. Deng, *J. Mater. Chem. A* **2015**, *3*, 7732-7740.

30   H. Heli, H. Yadegari, A. Jabbari, *J. Phys. Chem. C.* **2011**, *115*, 10889-10897.

31   M. Quintin, O. Devos, M. H. Delville, G. Campet, *Electrochim. Acta* **2006**, *51*, 6426-6434.

32   X. N. Li, X. B. Zhu, J. W. Liang, Z. G. Hou, Y. Wang, N. Lin, Y. C. Zhu, Y. T. Qian, *J. Electrochem. Soc.* **2014**, *161*, A1181-A1187.

33   W. Wu, J. Y. Yan, A. Wise, A. Rutt, J. F. Whitacre, *J. Electrochem. Soc.* **2014**, *161*, A561-A567

34   G. Pang, C. Z. Yuan, P. Nie, B. Ding, J. J. Zhu, X. G. Zhang, *Nanoscle*, **2014**, *6*, 6328-6334.

35   M. Vujkovic, M. Mitric, S. Mentus, *J. Power Sources*, **2015**, *288*, 176-186.

5 36   J. F. Whitacre, A. Tevar, S. Sharma, *Electrochem. Commun.* **2010**, *12*, 463-466.

Nanoscale Accepted Manuscript